Table I. Characteristics of polyclonal and monoclonal antibodies to the putative HCV E2 glycoprotein.

Antibody	ELISA[a] titer	IFA[b] titer	WB[c] titer	Epitope[d] (amino acid position)[e]
Polyclonal				
RR6	10^6	$\geq 10^3$	$\geq 10^3$	
Monoclonal				
747	<0.1 μg/ml	<10 μg/ml	< 1 μg/ml	520-540
843	<0.1 μg/ml	<10 μg/m	<10 μg/ml	520-540
1518	<0.1 μg/ml	<10 μg/ml	<10 μg/ml	450-470
1671	<0.1 μg/ml	<10 μg/ml	<10 μg/ml	640-660
1864	<0.1 μg/ml	<0 μg/ml	<1 μg/ml	450-470

[a]Carried out using synthetic peptides and purified recombinant HCV E2 glycoproteins. [b]Performed using recombinant vaccinia virus- and baculovirus-infected cells. [c]Western blot analysis, using purified recombinant glycoproteins from the putative E2 glycoprotein region of HCV genotype 1b. [d]Mapped using 20-amino acid oligopeptides, each overlapping the adjacent oligopeptide by 10 amino acids. [e]Kato *et al* (7).

mouse monoclonal antibodies (159, 260, 305 and 1905) to the HCV E1 glycoprotein were described previously (13).

Electron microscopy and immunogold electron microscopy. For conventional EM, 3 μl of each virus sample was applied to formvar-coated and carbon-vaporized grids and then negatively stained with 2% phosphotungstic acid, pH 6.5. The grid was examined under a Hitachi H-800 electron microscope operated at 100 kV. Indirect immunogold EM was performed as previously described (13-17). In brief, 3 μl of each virus sample was adsorbed on the grid and then the semidried grid was floated for 5 min on a drop of TBS-BSA (100 mM Tris-HCl, pH 7.6, 150 mM NaCl, and 2% bovine serum albumin) placed on parafilm in a moist chamber. The grid was then floated for 30 min on a drop of TBS containing 3% gelatin and then the excess gelatin from the drop of TBS-BSA was washed away. The grid was incubated for 60 min on a drop of primary antibody solution (diluted 1:100 in TBS-BSA) at room temperature, and then washed three times with TBS-BSA. After incubating the grid for 60 min in a drop of secondary antibody solution (diluted 1:20 in TBS-BSA), the grid was washed three times with TBS-BSA and once with TBS. The grid was negatively stained with 2% phosphotungstic acid for EM observation. Indirect immunogold EM was performed using rabbit anti-HCV E2 antibody RR6 at a dilution of 1:100 or a mixture of five monoclonal anti-HCV E2 antibodies (747, 843, 1518, 1671 and 1864), at a dilution of 1:10 as a primary antibody, and goat anti-rabbit IgG colloidal gold particles (10 nm in diameter; BioCell Research Laboratories, Cardiff, UK) or staphylococcal Protein A-conjugated colloidal gold particles (5 nm in diameter, BioCell Research Laboratories) as a secondary antibody. HCV particles (genotype 1b, 10^8 copies/ml of HCV RNA) in 1.14-1.16 g/ml sucrose fractions were incubated on carbon-coated copper grids with RR6 at a dilution of 1:100 and with a mixture of five clones of mouse anti-HCV E2 monoclonal antibodies at a dilution of 1:10. The HCV E1 and E2 glycoproteins on the virion were double labeled as follows. HCV particles were initially incubated with a mixture of four clones of mouse anti-HCV E1 monoclonal antibodies (159, 260, 305 and 1905) at a dilution of 1:10 and protein A-conjugated 5 nm-gold particles at a dilution of 1:20. Then, the sample was treated with rabbit anti-HCV E2 polyclonal antibody (RR6) at a dilution of 1:100 and with goat anti-rabbit IgG-conjugated 10 nm-gold particles at a dilution of 1:20. Finally, the samples were stained with 2% phosphotungstic acid for EM observation. In addition, HCV particles were initially incubated with a mixture of five clones of mouse anti-HCV E2 monoclonal antibodies (747, 843, 1518, 1671, and 1864) at a dilution of 1:10 and protein A-conjugated 5 nm-gold particles at a dilution of 1:20, and then reacted with the rabbit anti-HCV E1 polyclonal antibody (RR2) at a dilution of 1:100 and with goat anti-rabbit IgG-conjugated 10 nm-gold particles at a dilution of 1:20. Finally, the samples were stained with 2% phosphotungstic acid.

Results

Localization of the HCV E2 glycoprotein on the surface of the virion. HCV-like particles (55-65 nm) with fine 6 nm spikes were visualized in sucrose fractions at a density of 1.14-1.16 g/ml from samples A and B (13). The HCV-like particles of 55-65 nm in diameter showing specific gold labeling when treated with the rabbit polyclonal anti-HCV E2 antibody are shown in Fig. 2A and B. Antibody haloes and their specific binding to goat anti-rabbit IgG colloidal gold particles (10 nm) can be observed in samples A (Fig. 2A) and B (Fig. 2B) but not in sample C or D. Antibody haloes and specific gold labeling were not observed when the normal rabbit serum and the anti-vaccinia virus Lister strain serum was used as the primary antibody in samples A (Fig. 2C) and B. The mixture of five clones of anti-HCV E2 antibodies (159, 260, 305 and 1905) also produced specific gold labeling of an HCV-like particle (Fig. 2D and E). This type of specific reaction was confirmed in samples A (Fig. 2D) and B (Fig. 2E) but not in sample C or D. In Fig. 2D an HCV particle with a visible inner core structure of 35 nm in diameter was also labeled with staphylococcal Protein A conjugated gold

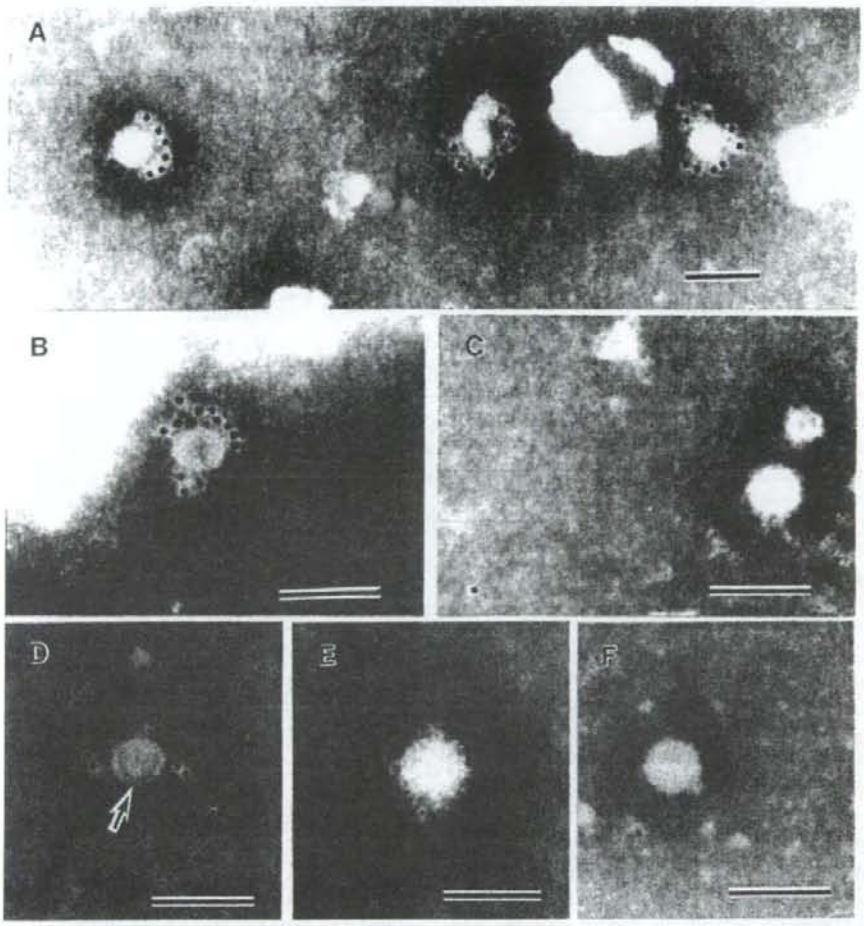

Figure 2. Immunogold electron micrographs of 55-65 nm HCV particles using rabbit polyclonal anti-HCV E2 antibody (RR6) and monoclonal anti-HCV E2 antibodies. HCV-like particles from sample A in (A), (C) and (E), and sample B in (B), (D) and (F) are shown. In (A) and (B), HCV-like particles were reacted with RR6 at a dilution of 1:100, and their antibody haloes were identified by binding to goat anti-rabbit IgG-conjugated colloidal gold particles (10 nm) at a dilution of 1:20. (C) Controls were prepared using rabbit polyclonal antibody to vaccinia virus Lister strain at a dilution of 1:100, following reaction with goat anti-rabbit IgG colloidal gold particles (10 nm) at a dilution of 1:20. In (D) and (E), HCV-like particles were reacted with a mixture of five monoclonal anti-HCV E2 antibodies, at a dilution of 1:10 and staphylococcal Protein A-conjugated colloidal gold particles (5 nm) at a dilution of 1:20. Specific labeling of gold particles on the surface of HCV-like particles can be noted. (D) An HCV-like particle with a visible inner core (indicated by an arrow) can be detected. (F) Controls were prepared using mouse monoclonal antibody to human blood type A antigen. The bars, 100 nm.

particles (5 nm). No specific gold labeling occurred in the presence of mouse monoclonal antibody to human blood type A antigen (Fig. 2F). The HCV-like particles specifically reacted with polyclonal and monoclonal antibodies to the HCV E2 glycoprotein.

Colocalization of the HCV E1 and E2 glycoproteins on the virion surface. When double labeling with different size colloidal gold was performed using monoclonal HCV E1 antibodies and the rabbit anti-HCV E2 polyclonal antibody (RR6), both staphylococcal Protein A-conjugated colloidal gold particles (5 nm) and goat anti-rabbit IgG colloidal gold particles (10 nm) were observed on the surface of the 55 nm HCV particle (Fig. 3A). Moreover, double labeling using the monoclonal HCV E2 antibodies and the rabbit anti-HCV E1 polyclonal antibody (RR2) also produced specific 5 nm and 10 nm gold labeling (Fig. 3B). Specificity of the immunogold labeling was confirmed using the mouse monoclonal antibody to the human blood type A antigen and protein A-conjugated colloidal gold particles (5 nm), and then using rabbit polyclonal antibody to vaccinia virus Lister strain and goat anti-rabbit IgG colloidal gold particles (10 nm) as negative controls, or by omitting the primary antibody. These negative control tests showed no specific gold labeling in 55-65 nm HCV-like particles with delicate surface spike-like projections (Fig. 3C). Both the HCV E1 and E2 glycoproteins colocalized on the surface of HCV virion.

Discussion

Recently, two *in vitro* HCV replication systems have been developed using an infectious HCV genotype 1b cDNA (23)

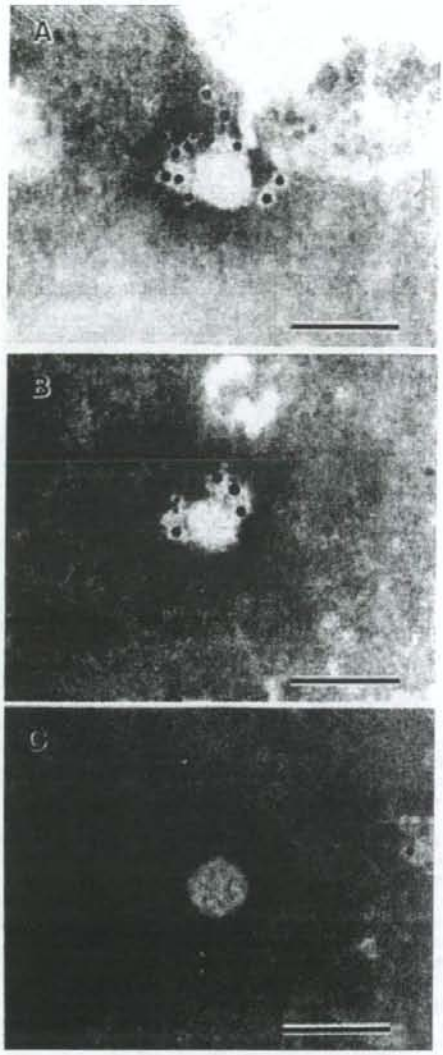

Figure 3. Immunogold electron micrographs of 55-65 nm HCV particles by double labeling with anti-HCV E1 and anti-HCV E2 antibodies. HCV-like particles from sample A are shown. (A) HCV-like particles were treated with a mixture of four monoclonal anti-HCV E1 antibodies at a dilution of 1:10 and staphylococcal Protein A-conjugated colloidal gold particles (5 nm) at a dilution of 1:20, and then with rabbit polyclonal anti-HCV E2 antibody (RR6); antibody haloes were identified by treating with goat anti-rabbit IgG-conjugated colloidal gold particles (10 nm) at a dilution of 1:20. (B) An HCV particle was detected using a mixture of five monoclonal anti-HCV E2 antibodies at a dilution of 1:10 and protein A-conjugated colloidal gold particles (5 nm) at a dilution of 1:20, and rabbit polyclonal anti-HCV E1 antibody (RR2) at a dilution of 1:100 and goat anti-rabbit IgG-conjugated colloidal gold particles (10 nm) at a dilution of 1:20. (C) Controls were prepared using mouse monoclonal antibody to human blood type A antigen at a dilution of 1:10, followed by treatment with Protein A-conjugated colloidal gold particles (5 nm) at a dilution of 1:20, treatment with rabbit polyclonal antibody to vaccinia virus Lister strain at a dilution of 1:100, and with goat anti-rabbit IgG colloidal gold particles (10 nm) at a dilution of 1:20. The bars, 100 nm.

and subgenomic replicons of the JFH1 genotype 2a strain (24). Heller *et al* (23) described an *in vitro* HCV replication system that is capable of producing viral particles in culture medium. A full-length HCV construct, CG1b of genotype 1b, known to be infectious (25), was placed between two ribozymes designed to generate the exact 5' and 3' ends of HCV after cleavage. After transfection into a human hepatoma cell line (Huh7), HCV-like particles, approximately 50 nm in diameter, increased in number and secreted into the culture medium. Sucrose density gradient centrifugation of the culture medium revealed colocalization of HCV RNA and structural proteins in a fraction at a density of 1.16 g/ml. HCV-like particles were observed in a fraction at a density of 1.16 g/ml. Wakita *et al* (24) developed subgenomic replicons of the HCV genotype 2a JFH1 strain cloned from an individual with fulminant hepatitis (26). After transfection into Huh7 cells, HCV particles, of approximately 55 nm in diameter, increased in number and secreted into the culture medium. These particles had a density of 1.15-1.17 g/ml in a 10-60% sucrose density gradient. HCV particles with an electron-dense inner core of 30-35 nm in diameter were identified by immunogold EM using monoclonal anti-HCV E2 antibody. Both studies showed that free HCV particles were about 55 nm spherical particles, had a density of about 1.16 g/ml and a 30-35 nm inner core. The morphology and the density of free HCV particles were quite consistent with our previous study (13). In Fig. 2, we demonstrate that the HCV E2 glycoprotein localized on the surface of 55-65 nm HCV particles containing a 30-35 nm inner core. The indirect immunogold electron microscopy detected immuno-gold-labeling in anti-HCV E2 antibody haloes surrounding the virions; haloes were produced by antigen-antibody reactions on the surface of virus-like particles, and they are good markers to discriminate HCV particles from other particles. In this way, the morphology of HCV virion can also be elucidated. Furthermore, our structural analysis of the HCV E1 and E2 envelope glycoproteins on HCV virions revealed that both HCV E1 and E2 envelope glycoproteins colocalize on the surface of virions in human plasma samples (Fig. 3).

The envelope glycoproteins have been shown to assemble into a noncovalent E1E2 heterodimer that is retained in the endoplasmic reticulum (27). This heterodimer is believed to be the prebudding form of an HCV glycoprotein complex (28). The E1E2 complex has been proposed as a functional subunit of HCV virions (11,12), and the E1E2 heterodimer is thought to be the functional unit of the HCV spike; low pH may induce dissociation leading to homooligomerization of the active form of the fusion protein (29,30). To date, it is known that both HCV E1 and E2 envelope glycoproteins are essential for receptor binding, host-cell entry, and membrane fusion (31,32). The HCV E2 glycoprotein also contains the binding site for CD81, a tetraspanin expressed on hepatocytes and B lymphocytes; CD81 is thought to function as a cellular receptor or coreceptor for the virus (33). Among the cellular factors mediating HCV entry into hepatocytes are tetraspanin CD81 (34-38), the human scavenger receptor SR-B1 (38,39), and probably the receptor for low density lipoproteins (40,41). However, the precise role of each receptor in HCV entry is still unclear and no vaccine is presently available. Further morphological studies on the binding site for CD81, the receptor SR-B1, and the receptor for low density lipoproteins of HCV virions from human plasma samples should be carried out.

In conclusion, both the HCV E1 and E2 glycoproteins are simultaneously present on the surface of the virion, providing definitive evidence that both the E1 and E2 envelope glycoproteins constitute the outer coat of fine spike-like projections of the HCV particle.

Acknowledgement

This study was supported in part by Grants-in Aid for Scientific Research (no. 17590632) from the Ministry of Education, Science and Culture of Japan, and from Specially Promoted Research on Viral Disease from the Tokyo Metropolitan Government.

References

1. Lauer GM and Walker BD: Hepatitis C virus infection. N Engl J Med 345: 41-52, 2001.
2. Lindenbach BD and Rice CM: *Flaviviridae*: the viruses and their replication. In: Fields Virology. Knipe DM and Howley PM (eds). Lippincott Williams & Wilkins, Philadelphia, pp991-1042, 2001.
3. Alter MJ: Epidemiology of hepatitis C. Hepatology 26 (Suppl 1): 62-65, 1997.
4. Montella M, Crispo A, Izzo F, *et al*: HCV and hepatocellular carcinoma: A case-control study in an area of hyperendemicity. Int J Mol Med 6: 571-574, 2000.
5. Fanning LJ: The Irish paradigm on the natural progression of hepatitis C virus infection: an investigation in a homogeneous patient population infected with HCV 1b. Int J Mol Med 9: 179-184, 2002.
6. Nagao Y, Tanaka K, Kobayashi K, Kumashiro R, Sata M: A cohort study of chronic liver disease in an HCV hyperendemic area of Japan: a prospective analysis for 12 years. Int J Mol Med 13: 257-265, 2002.
7. Kato N, Hijikata M, Ootsuyama Y, *et al*: Molecular cloning of the human hepatitis C virus genome from Japanese patients with non-A non-B hepatitis. Proc Natl Acad Sci USA 87: 9524-9528, 1990.
8. Takamizawa A, Mori C, Fuke I, *et al*: Structure and organization of the hepatitis C virus genome isolated from human carriers. J Virol 65: 1105-1113, 1991.
9. Reed KE and Rice CM: Overview of hepatitis C virus genome structure, polyprotein processing, and protein processing, and protein properties. Curr Top Microbiol Immunol 244: 55-84, 2000.
10. Kohara M, Tsukiyama-Kohara K, Maki N, *et al*: Expression and characterization of glycoprotein gp35 of hepatitis C virus using recombinant vaccinia virus. J Gen Virol 73: 2313-2318, 1992.
11. Dubuisson J, Hsu HH, Cheung RC, Greenberg HB, Russell DG and Rice CM: Formation and intracellular localization of hepatitis C virus envelope glycoprotein complexes express by recombinant vaccinia and Sindbis viruses. J Virol 68: 6147-6160, 1994.
12. Ralston R, Thudium K, Berger K, *et al*: Characterization of hepatitis C virus envelope glycoprotein complexes expressed by recombinant vaccinia viruses. J Virol 67: 6753-6761, 1993.
13. Kaito M, Watanabe S, Tsukiyama-Kohara K, *et al*: Hepatitis C virus particle detected by immunoelectron microscopic study. J Gen Virol 75: 1755-1760, 1994.
14. Watanabe S, Kaito M and Kohara M: Immunoelectron microscopic characterization of HCV. In: Methods in Molecular Medicine, vol. 19: Hepatitis C protocols. Lau JYN (ed). Humana Press, Totowa, NJ, pp279-285, 1998.
15. Fujita N, Kaito M, Ishida S, *et al*: Paraformaldehyde protects of Hepatitis C Virus particles during ultracentrifugation. J Med Virol 63: 108-116, 2001.
16. Kaito M, Watanabe S, Kohara M, Tsukiyama-Kohara K, Ishida S, Takeo M, Tanaka H, Horiike S, Naoki F, Iwasa M, Gabazza EC, Ikoma J and Adachi Y: Hepatitis C virus particles detected by immunogold electron microscopy. In: Science, Technology and Education of Microscopy: an Overview. Mendez-Vilas A (ed). Vol. 2, Formatex, Badajoz, pp490-498, 2003.
17. Ishida S, Kaito M, Kohara M, *et al*: Hepatitis C virus core particle detected by immunoelectron microscopy and optical rotation technique. Hepatol Res 20: 335-347, 2001.
18. Simmonds P, McOmish F, Yap PL, *et al*: Sequence variability in the 5' non-coding region of hepatitis C virus: identification of a new virus type and restrictions on sequence diversity. J Gen Virol 74: 661-668, 1993.
19. Kaneko S, Murakami S, Unoura M and Kobayashi K: Quantitation of hepatitis C virus RNA by competitive polymerase chain reaction. J Med Virol 37: 278-282, 1992.
20. Yoshioka K, Kakumu S, Wakita T, *et al*: Detection of hepatitis C virus by polymerase chain reaction and response to interferon-α therapy: relationship to genotypes of hepatitis C virus. Hepatology 16: 293-299, 1992.
21. Fubahashi S, Itamura S, Iinuma H, Nerome K, Sugimoto M and Shida H: Increased expression *in vivo* and *in vitro* of foreign genes directed by A-type inclusion body hybrid promoters in recombinant vaccinia viruses. J Virol 65: 5584-5588, 1991.
22. Matsuura Y, Harada S, Suzuki R, *et al*: Expression of processed envelope protein of hepatitis C virus in mammalian and insect cells. J Virol 66: 1425-1431, 1992.
23. Heller T, Saito S, Auerbach J, *et al*: An *in vitro* model of hepatitis C virion production. Proc Natl Acad Sci USA 102: 2579-2583, 2005.
24. Wakita T, Pietschmann, Kato T, *et al*: Production of infectious hepatitis C virus in tissue culture from a cloned viral genome. Nat Med 11: 791-796, 2005.
25. Thomson M, Nascimbeni M, Gozales S, Murthy KK, Rehermann B and Liang TJ: Emergence of a distinct pattern of viral mutations in chimpanzees infected with a homogeneous inoculum of hepatitis C virus. Gastroenterology 121: 1226-1230, 2001.
26. Kato T, Furusaka A, Miyamoto M, *et al*: Sequence analysis of hepatitis C virus isolated from a fulminant hepatitis patient. J Med Virol 64: 334-339, 2001.
27. Deleersnyder V, Pillez A, Wychowski C, *et al*: Formation of native hepatitis C virus glycoprotein complexes. J Virol 71: 697-704, 1997.
28. Dubuisson J: Folding, assembly and subcellular localization of hepatitis C virus glycoproteins. Curr Top Microbiol Immunol 242: 135-148, 2000.
29. Op De Beeck A, Voisset C, Bartosch B, *et al*: Characterization of functional hepatitis C virus envelope glycoproteins. J Virol 78: 2994-3002, 2004.
30. Lavillette D, Bartosch B, Nourrisson D , *et al*: Hepatitis C virus glycoproteins mediated low pH-dependent membrane fusion with liposomes. J Biol Chem 281: 3909-3017, 2006.
31. Bartosch B, Dubuisson J and Cosset FL: Infectious hepatitis C pseudoviruses containing functional E1E2 envelope protein complexes. J Exp Med 197: 633-642, 2003.
32. Drummer HE and Poumbourios P: Hepatitis C virus glycoprotein E2 contains a membrane-proximal heptad repeat sequence that is essential for E1E2 glycoprotein heterodimerization and viral entry. J Biol Chem 279: 30066-30072, 2004.
33. Pileri P, Uematsu Y, Campagnoli S, *et al*: Binding of hepatitis C virus to CD81. Science 282: 938-941, 1998.
34. Yagnik AT, Lahm A, Meola A, *et al*: A model for the hepatitis C virus envelope glycoprotein E2. Proteins 40: 355-366, 2000.
35. Hsu M, Zhang J, Flint M, *et al*: Hepatitis C virus glycoproteins mediate pH-dependent cell entry of pseudotyped retroviral particles. Proc Natl Acad Sci USA 100: 7271-7276, 2003.
36. Cormier EG, Tsamis F, Kajumo F, Durso RJ, Gardner JP and Dragic T: CD81 is an entry coreceptor for hepatitis C virus. Proc Natl Acad Sci USA 101: 7270-7274, 2004.
37. Bartosch B, Vitelli A, Granier C, *et al*: Cell entry of hepatitis C virus requires a set of co-receptors that include the CD81 tetraspanin and the SR-B1 scavenger receptor. J Biol Chem 278: 41624-41630, 2003.
38. Zhang J, Randall G, Higginbottom A, Monk P, Rice CM and McKeaking JA: CD81 is required for hepatitis C virus glycoprotein-mediated viral infection. J Virol 78: 1448-1455, 2004.
39. Scarselli E, Ansuini H, Cerino R, *et al*: The human scavenger receptor class B type I is a novel candidate receptor for the hepatitis C virus. EMBO J 21: 5017-5025, 2002.
40. Agnello V, Abel G, Elfahal M, Knight GB and Zhang QX: Hepatitis C virus and other flaviviridae viruses enter cells via low density lipoprotein receptor. Proc Natl Acad Sci USA 96: 12766-12771, 1999.
41. André P, Komurian-Pradel F, Deforges S, *et al*: Characterization of low- and very-low-density hepatitis C virus RNA-containing particles. J Virol 76: 6919-6928, 2002.

Original Research

Imaging Living Mice Using a 1-T Compact MRI System

Yusuke Inoue, MD,[1*] Yukihiro Nomura, MS,[1] Tomoyuki Haishi, PhD,[2] Kohki Yoshikawa, MD,[3] Takahiro Seki, PhD,[4] Kyoko Tsukiyama-Kohara, PhD,[4] Chieko Kai, PhD,[4] Toshiyuki Okubo, MD,[1] and Kuni Ohtomo, MD[5]

Purpose: To determine the feasibility of imaging living mice with a 1-T compact MRI system and investigate appropriate imaging techniques for use in routine animal experiments.

Materials and Methods: An MRI system consisting of a 1-T permanent magnet and compact console was used. Images of the entire trunks of living mice were obtained on the system using a T1-weighted three-dimensional fast low-angle shot (3D FLASH) sequence, and image quality was evaluated in relation to imaging techniques.

Results: Restraint of respiratory motion improved the image quality. Decreasing the slice thickness reduced artificial inhomogeneity in signal intensity (SI). Substantial effects of TR and FA on image quality were also demonstrated. With the determined techniques, images covering the entire trunk with a voxel size of 0.26 × 0.26 × 0.52 mm were acquired in an acquisition time of five minutes 28 seconds and a total experiment time of <20 minutes, and various organs and subcutaneous tumors were clearly visualized.

Conclusion: The compact MRI system provides images of living mice with acceptable quality in a reasonable time. Considering its convenience, it appears to be suitable for use in routine mouse experiments.

Key Words: magnetic resonance imaging; mouse; 3D FLASH; imaging technique; permanent magnet
J. Magn. Reson. Imaging 2006;24:901–907.

MEDICAL IMAGING TECHNOLOGIES, including magnetic resonance imaging (MRI), computed tomography (CT), single photon emission computed tomography (SPECT), and positron emission tomography (PET), are increasingly used for small-animal experiments. Conventional methods of studying animal models require that the animals be killed, and do not allow for serial observations in a given animal. Noninvasive imaging permits investigators to perform short- or long-term repetitive assessments of an individual animal to study anatomical and functional changes related to such things as disease progression, therapeutic effect, and pharmacokinetics. Each animal can be used as its own control, leading to greater reliability of the obtained results even when a small number of animals are used.

MRI can provide three-dimensional (3D) information about both anatomy and function with no radiation exposure, and is recognized as a powerful modality for small-animal experiments (1–4). However, high cost and low research accessibility may preclude the use of MRI in routine experiments (4,5). For imaging small objects, such as mice, high spatial resolution is critically important. To obtain sufficient signal from a small voxel, instruments dedicated to small animals or small samples are commonly used. Such MRI units generally have a small bore and a superconducting magnet of high field strength (≥4 T). Although they can provide sufficient signal for high-resolution imaging, these units often require a large space for installation. Cryogen refills, which are needed to maintain the superconducting magnet, are troublesome, especially for a specific pathogen-free (SPF) animal facility that restricts entry to prevent biological contamination. Some authors have reported the use of a 1.5-T clinical scanner and a dedicated small-animal coil (6–8). However, the time available for animal experiments is limited on a clinical scanner, and imaging of disease-model animals on a clinical unit may cause cross-contamination between animals and patients.

Efforts have been made to improve systems using high-field superconducting magnets for convenience. The use of active shielding can depress the fringe magnetic field, and a refrigeration system can be installed to reduce the frequency of cryogen refills. A compact MRI system that uses a 1-T permanent magnet was recently developed, and high-resolution images of fixed mice were obtained (9). Both the magnet and console of the

[1]Department of Radiology, Institute of Medical Science, University of Tokyo, Tokyo, Japan.
[2]MRTechnology Inc., Tsukuba, Japan.
[3]Department of Radiotechnical Sciences, Faculty of Radiological Health Sciences, Komazawa University, Tokyo, Japan.
[4]Laboratory Animal Research Center, Institute of Medical Science, University of Tokyo, Tokyo, Japan.
[5]Department of Radiology, Graduate School of Medicine, University of Tokyo, Tokyo, Japan.
*Address reprint requests to: Y.I., Department of Radiology, Institute of Medical Science, University of Tokyo, 4-6-1 Shirokanedai, Minato-ku, Tokyo 108-8639, Japan. E-mail: inoueys-tky@umin.ac.jp
Received August 1, 2005; Accepted June 29, 2006.
DOI 10.1002/jmri.20713
Published online 12 September 2006 in Wiley InterScience (www.interscience.wiley.com).

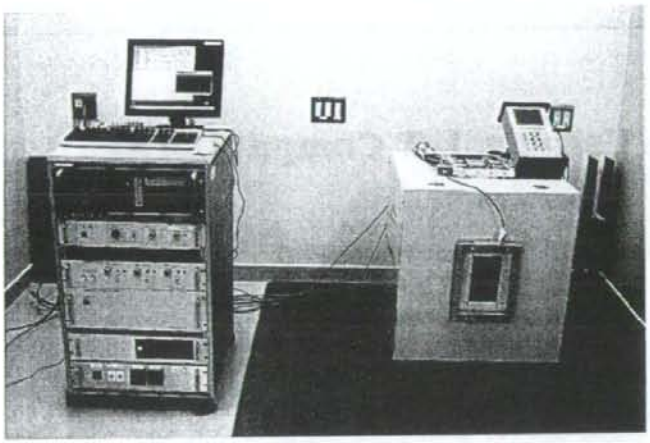

Figure 1. 1-T compact MRI system installed in the laboratory of an animal facility. The console (left) is placed in contiguity with the magnet (right).

system are small, and the fringe magnetic field is relatively weak. It can be installed in a small room that contains other electric or paramagnetic apparatuses. Cryogen refills are not needed, and the running cost is negligible. The openness of a permanent magnet system provides excellent accessibility to the sample in the magnet bore, which in turn makes it easy to position and monitor the sample. Because of these advantages, the system appears to be potentially applicable to routine small-animal experiments. In addition to high resolution, a short examination time is essential for routine experiments. The major problem is its relatively low magnetic field, which makes it difficult to achieve a sufficient signal-to-noise ratio (SNR) without excessive prolongation of the scan time because the magnetic field is a primary determinant of the SNR (10).

In this study we attempted to visualize living mice with the 1-T compact MRI system. We acquired images using a T1-weighted 3D fast low-angle shot (FLASH) sequence and investigated appropriate techniques to obtain images of acceptable quality in a reasonable imaging time. The principal aim of this study was to determine the applicability of the MRI system to routine experiments using mouse models.

MATERIALS AND METHODS

Instruments

Data were acquired on an MRmini system (MRTechnology, Tsukuba, Japan), consisting of a 1-T permanent magnet made of Nd-Fe-B material (Neomax, Osaka, Japan) and a compact console (Fig. 1). A solenoid coil of a 30-mm inner diameter was used. The specifications of the magnet were as follows: dimensions = 60 (W) × 64 (H) × 82 (D) cm, weight = 1400 kg, air gap = 10 cm, and magnetic field homogeneity = 3.6 ppm in a 30-mm diameter spherical volume. The maximum amplitude and slew rate of the gradient system were 70 mT/m and 350 T/m/second, respectively. The dimensions of the console were 52 (W) × 87 (H) × 60 (D) cm, and the total weight was about 100 kg. The horizontal 5-gauss line from the magnetic center was less than 1.2 m, and the entire system, including the console, was installed in a space of 1.5 × 3 m^2, without magnetic shielding, in the laboratory of an SPF animal facility.

Animals

Female wild-type BALB/c mice, BALB/c nude mice, and severe combined immunodeficiency (SCID) mice were used for the animal experiments. All mice weighed about 25 g and were given food and water ad libitum. They were handled according to the guidelines of the host institution, and the experiments were approved by the committee for animal research at the institution.

Imaging Procedures

The mice were anesthetized with isoflurane inhalation and fixed on a polymethylmethacrylate holder in the prone position. The mouse and holder were tightly wrapped together with paper tape to reduce respiratory motion artifact. Coronal images of the entire trunk were obtained using a T1-weighted 3D FLASH sequence as localizer images. The scan parameters were as follows: repetition time (TR) = 30 msec, echo time (TE) = 3.6 msec, flip angle (FA) = 36°, in-plane matrix = 256 × 64, 32 slab partitions, number of excitations = 1, bandwidth = 50 kHz, and acquisition time = one minute two seconds. The in-plane pixel size was 0.26 mm × 0.52 mm, and slice thickness was 1.04 mm. If necessary the position of the mouse was changed, followed by additional acquisition of localizer images. After appropriate positioning was confirmed, images of higher spatial resolution were obtained in the coronal plane using a T1-weighted 3D FLASH sequence. The in-plane matrix was 256 × 128, and the in-plane pixel size was 0.26 × 0.26 mm. The slab thickness was fixed irrespectively of the number of slab partitions, and the slice thickness was 0.52 mm at 64 partitions. The TE was set at 3.6 and 6.7 msec for out-of-phase and in-phase imaging, respectively. The number of excitations was set at one for all data acquisitions to reduce scan time, and the bandwidth was 50 kHz. Other parameters are presented in the following sections. Because the Larmor frequency of

a high-field permanent magnet circuit using Nd-Fe-B material is sensitive to alterations in temperature, it was measured just before each acquisition to compensate for temperature-dependent drift.

Restraint of Respiratory Motion

The effect of respiratory motion on image quality was evaluated. Two wild-type mice and two nude mice were imaged with and without restraint of respiratory motion, which was achieved by tightly wrapping the mouse and holder together with paper tape. Two mice were imaged without wrapping first, and the remaining two were imaged with wrapping first. The scan parameters were as follows: TR = 40 msec, TE = 3.6 msec and 6.7 msec, FA = 57°, 64 partitions, and acquisition time = five minutes 28 seconds.

Slab Partition

To determine the appropriate number of slab partitions, two wild-type mice were imaged with eight, 16, 32, 64, and 128 partitions, resulting in acquisition times of 42 seconds, one minute 23 seconds, two minutes 45 seconds, five minutes 28 seconds, and 10 minutes 56 seconds, respectively, and slice thicknesses of 4.16, 2.08, 1.04, 0.52, and 0.26 mm, respectively. Other parameters were TR = 40 msec, TE = 3.6 msec, and FA = 57°. For phantom studies, a 50-mL tube containing copper sulfate solution, a sphere, and meshes was imaged with the same sets of imaging parameters.

TR and FA

The effect of TR and FA on image quality was examined. First we imaged a wild-type mouse successively, without changing the position of the mouse, using various values of TR and FA. The TRs used were 30, 40, and 50 msec, and the FAs used were 71°, 64°, 51°, 36°, and 28°. Data were acquired with TEs of 3.6 and 6.7 msec, and a total of 30 sets of images were obtained. The partition number was 32. The acquisition times were two minutes three seconds, two minutes 45 seconds, and three minutes 26 seconds for TRs of 30, 40, and 50 msec, respectively.

Next, 64-partition images were acquired for three wild-type mice and three nude mice using various TRs and FAs. The parameters used were TEs of 3.6 and 6.7 msec; TRs of 40, 50, and 60 msec; FAs of 64°, 57°, and 51°; and a total of 18 image sets were obtained successively for each mouse. The acquisition times were five minutes 28 seconds, six minutes 51 seconds, and eight minutes 13 seconds for TRs of 40, 50, and 60 msec, respectively.

Subcutaneous Tumor Xenografts

Visualization of subcutaneous tumor xenografts was evaluated. Two SCID mice were implanted in the left flank with 1×10^6 cells of human hepatocellular carcinoma cell line (HT17) mixed with matrigel (BD Biosciences, San Jose, CA, USA). After the tumors became palpable, MRI was performed. Two perpendicular diameters of the tumor (a: longer diameter; b: shorter diameter) were measured manually with a caliper, and tumor volume was calculated as $V = (\pi/6)ab^2$. The tumor volumes for the two mice were 77.2 and 207.2 mm^3 on the day of MRI. The parameters used for MRI were TE = 3.6 and 6.7 msec, TR = 40 msec, FA = 57°, 64 partitions, and acquisition time = five minutes 28 seconds. In addition, an SCID mouse was implanted in the left flank with 1×10^6 cells of human hepatocellular carcinoma cell line (Hep 3B) mixed with matrigel. The initial imaging study, using the parameters described above, was performed five weeks after implantation, followed by weekly imaging.

Data Analysis

For all experiments the image quality was evaluated visually by two radiologists. The SNR for the liver was calculated in some experiments. Regions of interest (ROIs) were manually drawn within the liver on three slices, avoiding the inclusion of signal voids corresponding to intrahepatic vessels, and the mean signal intensity (SI) of the liver was calculated. A rectangular ROI was also placed for the background region, and the standard deviation (SD) of the SI in the ROI was determined as noise. The SNR of the liver was defined as the ratio of the mean liver SI to noise. For all imaging sessions of the three mice bearing subcutaneous tumor xenografts, tumor volume was determined from MR images obtained with a TE of 6.7 msec. The contour of the tumor was traced manually on each slice in which the tumor was visualized, and tumor volume was calculated by summing the products of areas measured on each slice and slice thickness.

RESULTS

Restraint of Respiratory Motion

Restraining respiratory motion by tightly wrapping the mouse and holder together definitely improved the image quality, and highlighted the significance of respiratory motion in distorting the quality of 3D FLASH images (Fig. 2). In the absence of restraint, artificial stripes were evident in the craniocaudal direction, especially on images obtained with a TE of 6.7 msec.

Slab Partition

The images of mice obtained using eight partitions were of poor quality. Data acquisition using 32 or more partitions, corresponding to a slice thickness of ≤1.04 mm, provided images of acceptable quality. The liver SNR was calculated for the images of 32 or more partitions, with increases in the number of partitions depressing the mean SNR (27.0, 19.1, and 15.1 for 32, 64, and 128 partitions, respectively). The 128-partition images were relatively noisy on visual evaluation; however, they visualized the contour of organs clearly because of their high cross-sectional resolution, and were considered to be of acceptable quality for use in routine experiments (Fig. 3). Imaging of the tube phantom with eight partitions produced severe artificial inhomogeneity even in the center slice. The inhomogeneity in phantom imag-

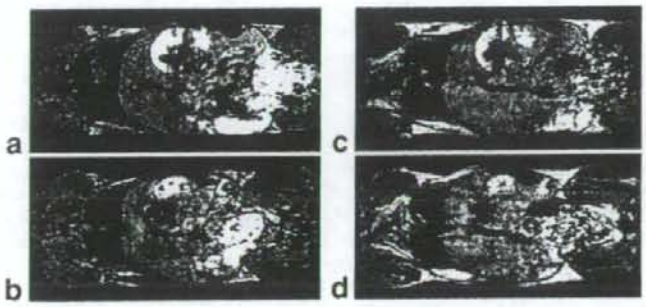

Figure 2. Coronal images of a mouse trunk obtained with (**a:** TE = 3.6 msec; **c:** TE = 6.7 msec) and without (**b:** TE = 3.6 msec; **d:** TE = 6.7 msec) restraint of respiratory motion. Artificial inhomogeneity in SI is reduced with restraint of respiratory motion. Signal void of the lung is displayed in the left part of each panel, and the pelvis is shown in the right part. The left side of the mouse is presented in the upper part of each panel.

ing was also reduced with increases in the number of partitions.

TR and FA

In imaging with 32 partitions and TE of 3.6 msec, a reduction in FA depressed the effect of noise visually but decreased image contrast (Fig. 4). Based on the balance between noise reduction and preservation of contrast, FA = 51–64° was judged to be appropriate. Longer TR also reduced the effect of noise at the expense of prolongation of acquisition time. Similar effects of TR and FA were shown for imaging with TE = 6.7 msec.

The SNRs for the liver on 64-partition images increased with increasing TR or decreasing FA (Fig. 5). Whereas a dependence of noise and contrast on TR and FA similar to that in 32-partition imaging was noted, each combination of TR and FA offered 64-partition images of acceptable quality in all mice. The liver, spleen, kidneys, lungs, heart, gallbladder, adrenal glands, ovaries, inguinal lymph nodes, and limb muscles were visualized (Fig. 6). Artificial inhomogeneity in the liver was often shown on images obtained with TE = 6.7 msec, and the liver was better delineated on images obtained with TE = 3.6 msec. The visualization of the kidneys was sometimes affected by artifacts that presumably were related to peristalsis, which was reduced with decreasing FA.

Subcutaneous Tumor Xenografts

In all three mice bearing subcutaneous tumor xenografts, the tumors were clearly delineated on images obtained with TE = 3.6 msec and 6.7 msec. They were well demarcated by hyperintense subcutaneous fat on

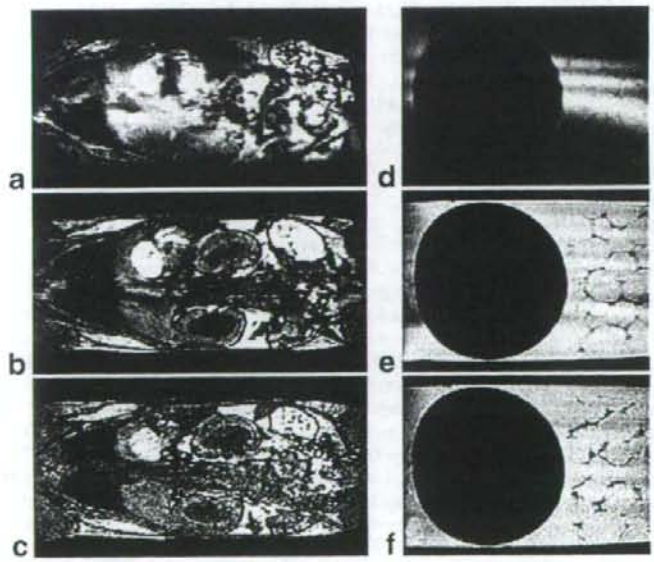

Figure 3. Mouse images obtained with eight (**a**), 32 (**b**), and 128 (**c**) partitions, and phantom images with eight (**d**), 32 (**e**), and 128 (**f**) partitions. Severe artificial inhomogeneities in SI are shown for the eight-partition images of both the mice and the phantom.

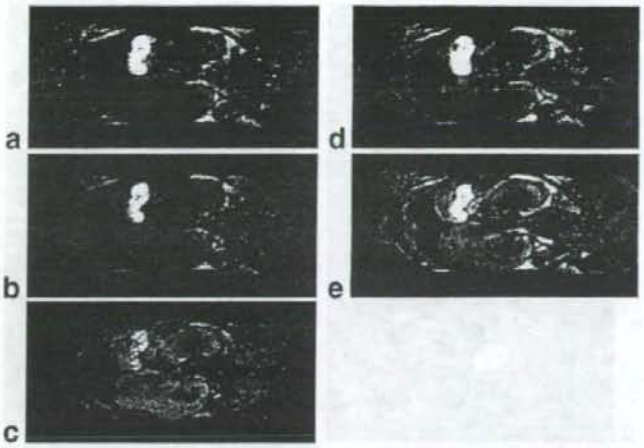

Figure 4. Effect of TR and FA in mouse imaging. Images were obtained with TR/FA = 40/71° (**a**), 40/51° (**b**), 40/28° (**c**), 30/51° (**d**), and 50/51° (**e**). A decrease in FA and increase in TR made the images less noisy; however, imaging with TR/FA = 40/28° yielded poor-contrast images.

images obtained with TE = 6.7 msec, resulting in easier recognition of the contours than on images obtained with TE = 3.6 msec. The tumor volumes obtained by the MR measurement (88.4 and 197.0 mm^3) were similar to those obtained by the caliper measurement (77.2 and 207.2 mm^3, respectively). In the mouse that was assessed serially, tumor growth was observed on the MR images visually and quantitatively (Fig. 7).

DISCUSSION

We examined the feasibility of imaging living mice on a 1-T compact MRI system and investigated appropriate imaging techniques. Although the system offers substantial convenience, the relatively low magnetic field impairs its ability to attain a high SNR (10). To overcome this problem, a small solenoid coil with many turns is used in the system because the SNR attained with a solenoid coil is approximately three times better than that attained with a saddle-shaped coil (10). The imaging sequence used was a 3D FLASH sequence, which can provide high-resolution, contiguous slices in a reasonable time (11,12). Motion artifacts may cause degradation of the 3D FLASH images in living subjects (11). We demonstrated that restraint of respiratory motion, achieved by a simple technique, definitely improves image quality. A FLASH sequence is sensitive to magnetic field inhomogeneities (13). Severe artifacts occurred when the phantom and mice were imaged with a small number of slab partitions, which apparently were attributable to intraslice inhomogeneity in the magnetic field enhanced by thickening of a slice. An increase in the partition number and consequent decrease in slice thickness reduced the artifact, and the image quality was acceptable when a slice thickness of ≤1.04 mm (32 or more partitions) was used. To achieve a sufficient SNR, preserved image contrast, and short acquisition time simultaneously, the effect of TR and FA on image quality was assessed, and appropriate values were defined. Using the determined parameters and techniques, we were able to obtain thin-slice 3D images covering the entire trunk of a mouse within a practical acquisition time and visualize various organs, including the liver, spleen, lung, and kidneys, consistently.

In this study the typical voxel size was 0.26 × 0.26 × 0.52 mm. Although images with higher in-plane resolution were acquired in some previous studies (14,15), in other studies the in-plane resolution was comparable to ours (6,16,17). Because we used a 3D sequence, the slice thickness, which is another important determinant of spatial resolution, was relatively thin. The spatial resolution required is dependent on the target of a particular study, and the spatial resolution in our study appears to be acceptable for various experimental

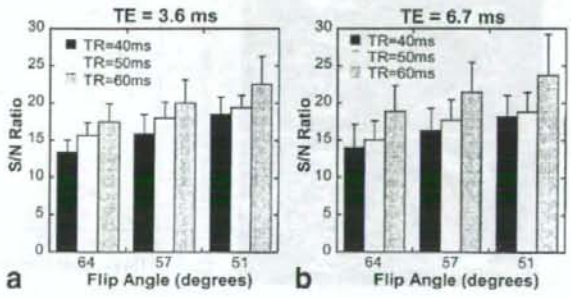

Figure 5. The SNR for the liver with TE = 3.6 (**a**) and 6.7 msec (**b**). The SNR increased with increasing TR and decreasing FA.

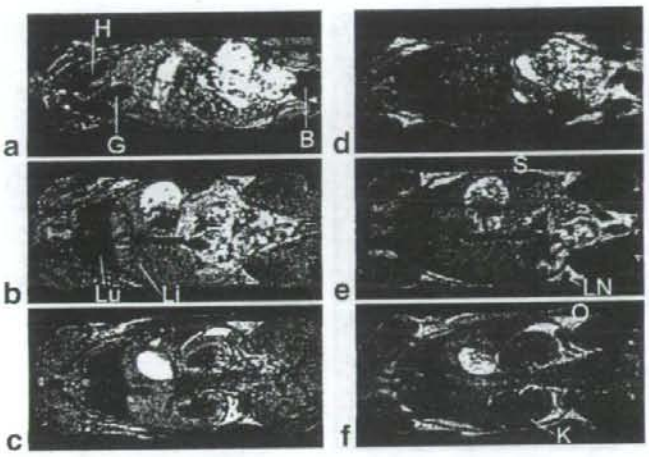

Figure 6. Images of a mouse obtained with TR/TE/FA = 40/3.6/57° (**a–c**) and 40/6.7/64° (**d–f**). H = heart, G = gallbladder, B = urinary bladder, Lu = lung, Li = liver, S = spleen, LN = inguinal lymph node, O = ovary, K = kidney.

applications. Spatial resolution can be improved at the expense of prolongation of scan time. However, routine laboratory experiments often require the use of many mice, and it is essential to acquire images of one mouse in a short time period. The imaging time required to cover the entire trunk with a spatial resolution of 0.26 × 0.26 × 0.52 mm was typically five minutes 28 seconds, and the total experiment time, from the start of induction of anesthesia to the end of data acquisition, was less than 20 minutes. The openness of a permanent magnet system, and placement of the magnet near other electric or paramagnetic apparatuses offer significant convenience for preparation, positioning, and monitoring of mice and operation of the instruments, which contributes to shortening the total experiment time and facilitating routine use of MRI.

Subcutaneous tumor xenografts were clearly visualized in this study. The volume of a subcutaneous tumor is commonly estimated by measuring two or three diameters manually with a caliper. The tumor volumes estimated from MRI were comparable to those obtained by the caliper measurement, and tumor growth could be followed on the MR images. The calculation of volume by the caliper measurement is based on the assumption of a simple shape and may be erroneous due to atypical morphology of a tumor (18). MRI delineates the entire tumor on thin-slice, contiguous images and does not require any geometric assumption for volume calculation. It appears to provide a reliable estimate of tumor volume irrespectively of the shape. While MRI is especially useful for visualizing internal organs and tumors located in deep sites, it may also aid in evaluating the morphology of subcutaneous tumors.

Versatility is one of the major advantages of MRI. Because the MR signal is influenced by a number of parameters, including proton density, T1 relaxation time, T2 relaxation time, magnetic susceptibility, water diffusion, and blood flow, images containing various kinds of anatomical and functional information can be acquired depending on the imaging sequences and parameters used. In this study we demonstrated the feasibility of T1-weighted FLASH imaging with the compact system, and its ability to visualize various organs and subcutaneous tumors. The applicability and utility of other imaging techniques using this system remain to be investigated. Experiments on microcirculation and cardiovascular function often require a combination of high temporal resolution and high spatial resolution, and it would be difficult to satisfy the requirements using the low-field system. The administration of contrast media also extends the usefulness of MRI. Intrinsic image contrast using a FLASH sequence is

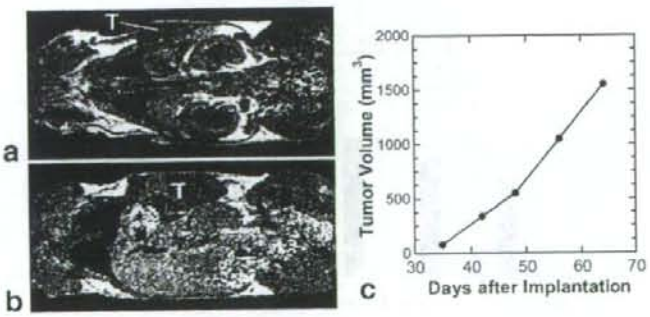

Figure 7. Images of a mouse bearing subcutaneous tumor xenograft (T) acquired five (**a**) and seven (**b**) weeks after implantation. The tumor volumes measured on MR images were plotted against the number of days after implantation (**c**).

lower than that obtained with a spin-echo sequence, and the use of contrast media is especially helpful in FLASH imaging (19). The contrast effect depends on the magnetic field strength (20), and the similarity in magnetic field between the compact MRI system and common clinical scanners may facilitate an exchange of information between clinical practice and experiments on the system.

In conclusion, we have demonstrated the feasibility of imaging living mice with a 1-T compact MRI system, and determined the appropriate imaging techniques. The system provides images of living mice with acceptable quality and within a reasonable time, and is expected to be useful for routine experiments on mouse models.

REFERENCES

1. Marzola P, Sbarbati A. Magnetic resonance imaging in animal models of pathologies. Methods Enzymol 2004;386:177–200.
2. Pautler RG. Mouse MRI: concepts and applications in physiology. Physiology (Bethesda) 2004;19:168–175.
3. Beckmann N, Mueggler T, Allegrini PR, Laurent D, Rudin M. From anatomy to the target: contributions of magnetic resonance imaging to preclinical pharmaceutical research. Anat Rec 2001;265:85–100.
4. Chatham JC, Blackband SJ. Nuclear magnetic resonance spectroscopy and imaging in animal research. ILAR J 2001;42:189–208.
5. Klaunberg BA, Lizak MJ. Considerations for setting up a small-animal imaging facility. Lab Anim (NY) 2004;33:28–34.
6. Kobayashi H, Kawamoto S, Brechbiel MW, et al. Micro-MRI methods to detect renal cysts in mice. Kidney Int 2004;65:1511–1516.
7. Smirnov P, Gazeau F, Lewin M, et al. In vivo cellular imaging of magnetically labeled hybridomas in the spleen with a 1.5-T clinical MRI system. Magn Reson Med 2004;52:73–79.
8. Gupta S, Adhami VM, Subbarayan M, et al. Suppression of prostate carcinogenesis by dietary supplementation of celecoxib in transgenic adenocarcinoma of the mouse prostate model. Cancer Res 2004 1;64:3334–3343.
9. Haishi T, Uematsu T, Matsuda Y, Kose K. Development of a 1.0 T MR microscope using a Nd-Fe-B permanent magnet. Magn Reson Imaging 2001;19:875–880.
10. Hoult DI, Richards RE. The signal-to-noise ratio of the nuclear magnetic resonance experiment. J Magn Reson 1976;24:71–85.
11. Ross JS, Masaryk TJ, Modic MT. Three-dimensional FLASH imaging: applications with gadolinium-DTPA. J Comput Assist Tomogr 1989;13:547–552.
12. Frahm J, Haase A, Matthaei D. Rapid three-dimensional MR imaging using the FLASH technique. J Comput Assist Tomogr 1986;10:363–368.
13. Winkler ML, Ortendahl DA, Mills TC, et al. Characteristics of partial flip angle and gradient reversal MR imaging. Radiology 1988;166:17–26.
14. Hensley HH, Chang WC, Clapper ML. Detection and volume determination of colonic tumors in Min mice by magnetic resonance micro-imaging. Magn Reson Med 2004;52:524–529.
15. Kobayashi H, Jo SK, Kawamoto S, et al. Polyamine dendrimer-based MRI contrast agents for functional kidney imaging to diagnose acute renal failure. J Magn Reson Imaging 2004;20:512–518.
16. Denis MC, Mahmood U, Benoist C, Mathis D, Weissleder R. Imaging inflammation of the pancreatic islets in type 1 diabetes. Proc Natl Acad Sci USA 2004 24;101:12634–12639.
17. Brooks BJ, Hill MD, Hockings PD, Reid DG. MRI detects early hindlimb muscle atrophy in Gly93Ala superoxide dismutase-1 (G93A SOD1) transgenic mice, an animal model of familial amyotrophic lateral sclerosis. NMR Biomed 2004;17:28–32.
18. Kiessling F, Heilmann M, Vosseler S, et al. Dynamic T1-weighted monitoring of vascularization in human carcinoma heterotransplants by magnetic resonance imaging. Int J Cancer 2003;104:113–120.
19. Runge VM, Wood ML, Kaufman D, Price AC. Gd DTPA. Future applications with advanced imaging techniques. Radiographics 1988;8:161–179.
20. Rinck PA, Muller RN. Field strength and dose dependence of contrast enhancement by gadolinium-based MR contrast agents. Eur Radiol 1999;9:998–1004.

Available online at www.sciencedirect.com
SCIENCE DIRECT
Comparative Immunology, Microbiology & Infectious Diseases 29 (2006) 157–165
COMPARATIVE IMMUNOLOGY & MICROBIOLOGY & INFECTIOUS DISEASES
www.elsevier.com/locate/cimid

Characterization of monoclonal antibodies directed against the canine distemper virus nucleocapsid protein

Munemitsu Masuda [a], Hiroki Sato [b], Hiroshi Kamata [c], Tomoe Katsuo [b], Akiko Takenaka [b], Ryuichi Miura [b], Misako Yoneda [b], Kyoko Tsukiyama-Kohara [b], Kiyohisa Mizumoto [a], Chieko Kai [b,*]

[a] *Department of Biochemistry, School of Pharmaceutical Sciences, Kitasato University, Shirokane, Minato-ku, Tokyo 108-8641, Japan*
[b] *Laboratory of Animal Research Center, Institute of Medical Science, University of Tokyo, 4-6-1 Shirokanedai, Minatoku, Tokyo 108-8639, Japan*
[c] *Department of Veterinary Medicine, College of Bioresource Sciences, Nihon University, Kameino 1866, Fujisawa, Kanagawa 252-8510, Japan*

Accepted 9 March 2006

Abstract

We have established four monoclonal antibodies (MAbs) against the nucleocapsid protein (NP) of canine distemper virus (CDV). A competitive binding assay has revealed that the MAbs are directed against two antigenic domains. An immunofluorescence assay using a series of deletion clones of the NP and an immunoprecipitation assay using the NP have revealed that two of the MAbs recognize the C-terminal region of the NP while the other two recognize the tertiary structure of the N-terminal domain. These MAbs reacted with all eight strains of CDV used in this study, but showed different reactivities against measles virus and rinderpest virus.

Keywords: Canine distemper virus; Nucleocapsid protein; Monoclonal antibodies; Deletion mutants; Antigenic domain; Competitive ELISA

* Corresponding author. Tel.: +81 3 5449 5497; fax: +81 3 5449 5397.
E-mail address: ckai@ims.u-tokyo.ac.jp (C. Kai).

0147-9571/$ - see front matter © 2006 Elsevier Ltd. All rights reserved.
doi:10.1016/j.cimid.2006.03.004

1. Introduction

Canine distemper virus (CDV) is a member of the genus *Morbillivirus* of the family *Paramixoviridae*. In all negative stranded RNA viruses, including the Paramyxoviruses, the genomic RNA is tightly bound to the nucleocapsid protein (NP), the major structural protein, in the form of a helical nucleocapsid [1]. This structure is a template required for both replication and transcription and comprises the ribonucleoprotein complex in conjunction with the viral large protein (L) and phosphoprotein (P) [2]. NPs are the most abundant viral proteins and highly conserved in the genus *Morbillivirus* [1]. Recently, the number of dogs showing typical clinical signs of CDV infection has been increasing, despite the fact that most of these dogs had been vaccinated [3]. Genetic variations in the *NP* gene have notably found in the field isolates [4]. It is therefore important for the characterization of recent field isolates of CDV to investigate the antigenic domains and genetic variations in the *CDV-NP* gene. However, only a few reports about preparation and characterization of monoclonal antibodies against CDV-NP have been reported previously [5,6], and only limited numbers of them are currently available for antigenic studies of CDV. In this study, we newly established four monoclonal antibodies (MAbs) against the NP of CDV-Onderstepoort strain and determined the antigenic regions of these antibodies by competitive binding assay and immunofluorescence assay (IFA). In addition, we compared these MAbs with the two MAbs against the NP of CDV-FXNO strain, which were previously established by Hirayama et al. [6]. Furthermore, we examined the reactivity of the four MAbs with other strains of CDV as well as those of other morbilliviruses, namely, measles virus (MV) and rinderpest virus (RPV).

2. Material and methods

2.1. Cells and virus

Vero cells were cultured in Dulbecco's modified Eagle's medium (DMEM) supplemented with 100 U/ml of penicillin G, 100 μg of streptomycin (GIBCO BRL, USA), and 5% fetal bovine serum (FBS; SIGMA, USA). COS-7 cells were cultured in a culture medium whose composition was the same as above except that it contained 10% FBS. B95a cells were cultured in RPMI-1640 medium supplemented with 100 U/ml of penicillin G, 100 μg of streptomycin, and 5% FBS. Five strains (Onderstepoort, FXNO, YSA, Snyder–Hill, and haku93) of CDV, the Edmonston strain of MV, the RBOK strains of RPV were propagated in Vero cells. Three strains (Yanaka, tanu, haku00) of CDV, the HL strain of MV, the L strain of RPV were propagated in B95a cells.

2.2. Hybridoma production and MAb screening

CDV-infected Vero cells showing 80–90% cytopathic effects (c.p.e.) were harvested, frozen and thawed, sonicated at 20 kHz for 30 s and clarified by centrifugation at 6000 rpm to prepare immunizing materials. MAbs were produced as described previously [7] with some modifications. Briefly, spleen cells obtained from CDV-immunized

BALB/c mice were fused with myeloma cells using polyethylene glycol 4000. The hybridoma cells were screened for antibody production against CDV using an indirect immunoperoxidase (IIP) test. Positive cells were cloned by the limiting dilution method and were inoculated intraperitoneally into pristane-primed BALB/c mice. For comparing with the four MAbs isolated in this study, MAbs c-5 and h-6 against the NP of CDV-FXNO strain [6] were used.

2.3. Radioimmunoprecipitation assay

The specificity of the MAbs was determined by radioimmunoprecipitation assay (RIPA) as described previously [8]. Briefly, virus-infected cells or mock-infected cells were radiolabeled with 3 MBq/ml[^{35}S]methionine and cystein (Amersham Bioscience) for 2 h. The cells were lysed with lysis buffer (0.5% TritonX-100, 0.5% sodium deoxycholate, and 5 mM NaCl). An aliquot of cell lysate was subjected to thermal denaturation by boiling for 5 min and was then reacted with the anti-NP MAbs for 3 h at 4 °C, followed by incubation with protein A beads. The immunoprecipitates were resolved by 10% SDS-polyacrylamide gel electrophoresis (SDS-PAGE).

2.4. Competitive binding assay

Antibodies (IgG) were precipitated in the ascitic fluid from hybridoma-inoculated mice containing 33% ammoniumsulphate precipitation and were then dialyzed against phosphate buffered saline (PBS). The IgG was biotinylated using a biotin labeling kit (Roche) according to the manufacture's instructions. Vero cells which had been infected with the Onderstepoort strain of CDV and showed 70–80% c.p.e. in 100-mm diameter culture dishes were lysed with 0.5 ml of lysis buffer (0.5% TritonX-100, 0.5% sodium deoxycholate, and 5 mM NaCl) and centrifuged at 5000 rpm for 3 min. Ninety-six-well microplates were coated with the supernatant for 1 h at room temperature as viral antigens for ELISA. An aliquot of the unlabeled MAbs was serially diluted fourfold, and aliquots of each dilution were placed in wells of the plates. After 1 h incubation at room temperature, the plates were washed three times with 0.05% Tween 20-PBS. A 0.05 ml aliquot of biotinylated MAb was diluted to an approximate OD of 0.1 added to each well and allowed to bind for 1 h at room temperature. The plates were washed three times again, followed by incubation with HRP-conjugated streptavidin (Roche) at a 1:1000 dilution for 1 h at room temperature. Then again the plates were washed three times and visualized with a TMB peroxidase EIA substrate kit (BIO-RAD) according to the manufacture's instructions. After 30 min, OD was measured at 655 nm with a microplate reader (BIO-RAD).

2.5. Construction and eukaryotic expression of NP and deletion mutants

Vero cells were inoculated with the Onderstepoort strain of CDV and were incubated for 18 h. Total RNA was then extracted using ISOGEN (Nippon Gene) according to the manufacture's instructions. One microgram of total RNA was reverse transcribed with SuperScript II reverse transcriptase (GIBCO BRL) in the presence of the antisence primer, P2 (1570–1587 nt position of *NP* gene). The resulting cDNA was amplified by PCR with

F1 sense primer (1–21 nt position of *NP* gene) and P2 antisence primer using LA-Taq DNA polymerase (TaKaRa). The amplified product was subcloned into pBluescript SK- vector, digested with *Xba* I and *Xho* I, and then inserted into pME-18S mammalian expression vector, designated as pME-ON. To create deletion clones of the NP, pME-ON was PCR amplified with a set of primers (described below) using *pfu turbo* DNA polymerase (Stratagene) according to the manufacture's instructions (NP-D1 sense 5′-gtggaatcccctggacaatt-3′, NP-D1 antisense 5′-catattggtaggtctgaacc-3′; NP-D2 sense 5′-atgaggagatggattaagtat-3′, NP-D2 antisense 5′-gaacaaggagaggatactgat-3′; NP-D3 sense 5′-atgatttgtgatatagataac-3′, NP-D3 antisense 5′-ctccgagtcggctgcagtatc-3′; NP-D4 sense 5′-atgggagttggtgttgaacttgaaaactca-3′, NP-D4 antisense 5′-ttcagcaattctaggcttgtt-3′; NP-D5 sense 5′-taaatattcaagaccagtcttgcatcagt-3′, NP-D5 antisense 5′-agcataactccagag-tagtgg-3′). PCR products were phosphorylated using a DNA kination kit (TOYOBO) and were self-ligated using a DNA ligation kit (TaKaRa). Nucleotide sequences of these constructs were confirmed by DNA sequencing (ABI PRISM 377 DNA sequencer).

COS-7 cells were seeded into 35-mm diameter culture dishes and grown until semi-confluent, and 1 μg of plasmid DNAs were transfected using FuGENE6 (Roche) according to the manufacture's instructions. After 24 h, cells were fixed with acetone and analyzed by indirect immunofluorescence assay (IFA) as described below.

2.6. IFA

Vero cells and B95a cells were infected with various strains of *Morbilliviruses* described above. When approximately 50% c.p.e. was observed, the cells were fixed with acetone for 30 min at room temperature, followed by incubation in a 1:1000 dilution of the ascitic fluids for 1 h at 37 °C. After washing in PBS, cells were incubated in a 1:500 dilution of fluorescein isothiocyanate (FITC)-conjugated anti-mouse IgG (ICN Biomedicals, Inc.) for 1 h at 37 °C. After washing in PBS, fluorescence was observed with a fluorescent microscope (Olympus).

3. Results

3.1. Specificity of the MAbs for CDV-NP

To obtain MAbs against the CDV-NP, mice were immunized with the Onderstepoort strain of CDV, and the hybridoma cells were established and screened, as described in Section 2. The specificity of the MAbs so obtained was determined by RIPA (Fig. 1). Four of the MAbs (2B, 7G, 8G, 3) detected a 58 kDa protein in the CDV-infected Vero cells. These results indicate that these four MAbs recognize the CDV-NP.

3.2. Analysis of the antigenic domains by competitive binding assay

To determine the antigenic domain(s) recognized by the four MAbs, we performed a competitive binding assay using the biotinylated MAbs. As shown in Table 1, two antigenic domains were identified: domain I was recognized by MAbs 2B and 3, and

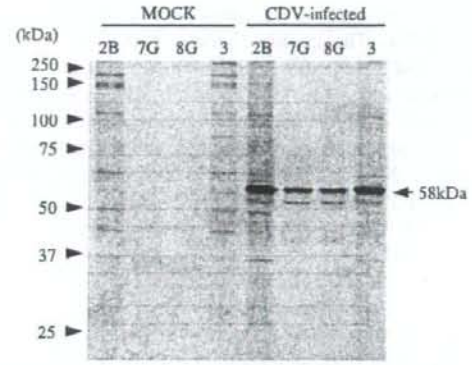

Fig. 1. Radioimmunoprecipitation assay (RIPA) of [^{35}S]methionine-labeled CDV viral proteins using MAbs. MOCK and CDV-infected Vero cells were metabolically labeled with ^{35}S-Met/Cys, then subjected to RIPA with MAb 2B, 7G, 8G, 3. The NP is indicated by arrow head (58 kDa).

domain II by MAbs 7G and 8G. Two other MAbs (c-5 and h-6), which were previously established by Hirayama et al. [6] and are directed against the NP of CDV-FXNO strain, were also tested by the same competitive binding assay. MAb h-6 recognized domain II in the same manner as MAbs 7G and 8G. On the other hand, MAb c-5 showed no competition with any other MAbs. MAb c-5 thus seems to recognize a distinct antigenic domain.

3.3. Mapping of the epitope regions in NP

To determine the epitope regions in the NP recognized by these MAbs, we constructed a series of deletion clones of the *NP* gene of the CDV Onderstepoort

Table 1
Analysis of the antigenic domains by competitive binding assay

Purified MAb	Antigenic domain	Biotinylated MAb					
		2B	3	7G	8G	h-6	c-5
2B	I	+[a]	+	−	−	−	−
3	I	+	+	−	−	−	−
7G	II	−	−	+	+	+	−
8G	II	−	−	+	+	+	−
h-6[b]	II	−	−	+	+	+	−
c-5[b]	III	−	−	−	−	−	+

A constant dilution of the biotinylated MAbs was incubated with a 1:4, 1:16, 1:64, 1:256 and 1:1024 dilution of each non-labeled MAb. Using the streptavidin HRP-conjugated, competition was determined as a reduction of the fixation of the conjugate by more than 80%.

[a] +, IFA positive; −, IFA negative.

[b] Previously reported MAb.

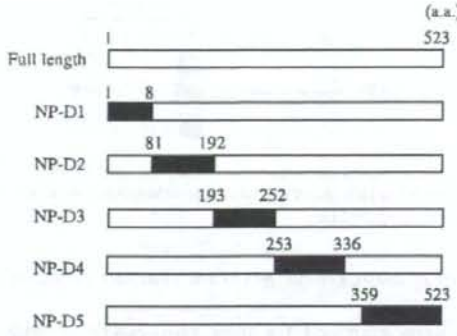

Fig. 2. *NP* gene and the series of its deletion clones of CDV strain Onderatepoort. These clones were inserted to eucaryotic expression vector pME-18S. The deleted regions of *NP* gene are indicated as filled bar. The number indicates amino acid residues.

strain as summarized in Fig. 2. These clones were expressed in COS-7 cells, and an IFA was performed using the four MAbs. MAbs 2B and 3 reacted with NP deletion clones D1 through D4 but not with D5 (Table 2). This suggests that MAbs 2B and 3 recognized the C-terminal region of the NP (a.a.359–523). Interestingly, this non-reactivity with NP-D5 is also shared by MAb c-5, which exhibited no competition with any other MAbs in the competitive binding assay. MAbs 7G, 8G and h-6 reacted only with NP-D5, indicating that they recognize an epitope on the protein expressed from the *NP* gene (a.a.1–336). However, none of NP clones D1 through D4 were recognized by these three MAbs. It is thus possible that these MAbs recognize the tertiary structure of the NP. To clarify this possibility, ^{35}S-labeled cell lysate infected with CDV was thermally denatured by boiling and was then subjected to RIPA. As shown in Fig. 3, the reactivity with the denatured NP was greatly reduced in MAbs 7G and 8G. These results indicate that MAbs 7G and 8G recognize the epitope in the NP's N-terminal domain which has a tertiary structure.

Table 2
Mapping of the epitope regions on NP

MAb	Control	Full length	D1	D2	D3	D4	D5
2B	−[a]	+	+	+	+	+	−
3	−	+	+	+	+	+	−
7G	−	+	−	−	−	−	+
s8G	−	+	−	−	−	−	+
h-6[b]	−	+	−	−	−	−	+
c-5[b]	−	+	+	+	+	+	−

[a] +, IFA positive; −, IFA negative.
[b] Previously reported MAb.

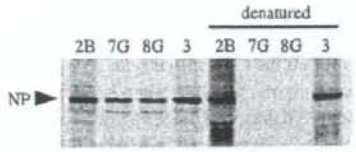

Fig. 3. RIPA with denatured or undenatured condition, using the four MAbs 2B, 7G, 8G 3. The immune complexes were electrophoresed in 10% SDS-PAGE and auto-radiographed by means of FUJIFILM BAS-1500. The NP is indicated by arrow head (58 kDa).

3.4. Immunoreactivity of anti-CDV NP MAbs with various strains of Morbillivirus

All four MAbs were examined for their cross-reactivity with various strains of *Morbilliviruses* using an IFA test. As summarized in Table 3, all MAbs reacted with all tested strains of CDV. In contrast, only MAbs 7G and 8G showed cross-reactivities with two strains (the Edmonston, HL) of MV and the RBOK strain of RPV, while MAbs 2B and 3 failed to show any cross-reactivity. None of the MAbs showed reactivity with the L strain of RPV.

4. Discussion

We obtained four MAbs directed against the NP of the CDV Onderstepoort strain. In the competitive binding assay, these four MAbs recognized a total of two antigenic domains. In addition, MAb c-5 against the NP of the CDV FXNO strain displayed no competition with any other MAbs. These results indicate that at least three distinct antigenic domains exist in the CDV-NP. The reactivities with the NP deletion clones revealed that MAbs 2B and 3

Table 3
Immunoreactivity of anti-CDV NP MAbs with various strains of *Morbillivirus*

Virus	Isolate/strain	Control	2B	3	7G	8G
CDV	Onderste-poort	−[a]	+	+	+	+
	YSA	−	+	+	+	+
	Snyder–Hill	−	+	+	+	+
	FXNO	−	+	+	+	+
	Yanaka	−	+	+	+	+
	Tanu	−	+	+	+	+
	Haku93	−	+	+	+	+
	Haku00	−	+	+	+	+
MV	Edmonston	−	−	−	+	+
	HL	−	−	−	+	+
RPV	RBOK	−	−	−	+	+
	L	−	−	−	−	−

[a] +, IFA positive; −, IFA negative.

recognize the C-terminal region of the NP (a.a.359–523). Interestingly, this reactivity with the C-terminal region of the NP is shared by MAb c-5, which recognized a unique antigenic domain. These results suggest that the C-terminal (a.a. 359–523) of the CDV-NP harbors at least two distinct antigenic domains. On the other hand, MAbs 7G and 8G showed no reactivity against four of the five deletion clones. In addition, after thermal denaturation of the NP, the reactivity with the NP disappeared in MAbs 7G and 8G. These results strongly suggest that antigenic domain I consists of the tertiary structure of the N-terminal region. Previous reports describe that the 400 N-terminal residues form a globular structure and that the C-terminal region appears to be a tail extending from the surface of the globular body [9–11]. It seems reasonable to explain that MAbs 7G and 8G recognize an epitope located on the surface of the globular structure of the NP.

All strains of CDV used in this study reacted with all four MAbs (2B, 7G, 8G and 3) (Table 3). In contrast, the Edmonston and HL strains of MV and the RBOK strain of RPV reacted with MAbs 7G and 8G but not with MAbs 2B and 3. The N-terminal 80% of the NP is highly conserved among the morbilliviruses [1]. The 400 N-terminal residues of the NP of the CDV Onderstepoort strain displayed 81.4, 81.2 and 81.5% homology to those of the MV Edmonston and HL strains and the RPV RBOK strain, respectively. On the other hand, the remaining C-terminal region of the NP is poorly conserved among the morbilliviruses [12]; the C-terminal region (a.a.400–523) of the NP of the CDV Onderstepoort strain has only 25.4, 25.6 and 26.4% homology to the equivalent NP regions of MV Edmonston and HL strains and the RPV RBOK strain, respectively. This variability in the C-terminal region may cause antigenic heterogeneity among morbilliviruses, which is in agreement with the results of this study. On the other hand, the L strain of RPV showed no reactivity with any of the four MAbs. This lapinized strain of RPV was derived from a wild-type strain after numerous passages through rabbits [13]. The homology between the NP of the CDV Onderstepoort strain and that of the RPV L strain is 68.0%. The antigenicity of the NP of RPV may be different from those of other morbilliviruses.

A previous report demonstrated that in the family *Paramixoviridae* the C-terminal region of the NP interacts with the viral L and P proteins and controls viral genome replication and transcription [2]. On the other hand, the N-terminal globular domain of the NP interacts with viral genome after completion of the folding process [14]. Previously, Gombert et al. reported the kinetics of conformational maturation of MV-NP using a monoclonal antibody, which recognizes a conformational epitope on NP, and antiserum, which recognizes a less folded form of NP [14]. However, there is no report for MAbs, which recognize a conformational epitope on CDV-NP. In this study, we obtained MAbs that recognize the tertiary structure of the N-terminal region and linear epitopes in the C-terminal region of the CDV-NP. These MAbs are expected to be powerful tools for further detailed functional analysis of the CDV-NP.

Acknowledgements

This study was supported by a grant from the Bio-oriented Technology Research Advancement Institution (BRAIN), and a grant-in-aid from the Japanese Ministry of Education, Science, Culture, and Sports.

References

[1] Parks GD, Ward CD, Lamb RA. Molecular cloning of the NP and L genes of simian virus 5: identification of highly conserved domains in paramyxovirus NP and L proteins. Virus Res 1992;22(3):259–79.
[2] Horikami SM, Curran J, Kolakofsky D, Moyer SA. Complexes of Sendai virus NP-P and P-L proteins are required for defective interfering particle genome replication in vitro. J Virol 1992;66(8):4901–8.
[3] Gemma T, Watari T, Akiyama K, Miyashita N, Shin YS, Iwatsuki K, et al. Epidemiological observations on recent outbreaks of canine distemper in Tokyo area. J Vet Med Sci 1996;58(6):547–50.
[4] Shin Y, Mori T, Okita M, Gemma T, Kai C, Mikami T. Detection of canine distemper virus nucleocapsid protein gene in canine peripheral blood mononuclear cells by RT-PCR. J Vet Med Sci 1995;57(3):439–45.
[5] Orvell C, Sheshberadaran H, Norrby E. Preparation and characterization of monoclonal antibodies directed against four structural components of canine distemper virus. J Gen Virol 1985;66(Pt 3):443–56.
[6] Hirayama N, Senda M, Nakashima N, Takagi M, Sugiyama M, Yoshikawa Y, et al. Protective effects of monoclonal antibodies against lethal canine distemper virus infection in mice. J Gen Virol 1991;72(Pt 11): 2827–30.
[7] Sugiyama M, Minamoto N, Kinjo T, Hirayama N, Sasaki H, Yoshikawa Y, et al. Characterization of monoclonal antibodies against four structural proteins of rinderpest virus. J Gen Virol 1989;70(Pt 10): 2605–13.
[8] Yoshida E, Shin YS, Iwatsuki K, Gemma T, Miyashita N, Tomonaga K, et al. Epitopes and nuclear localization analyses of canine distemper virus nucleocapsid protein by expression of its deletion mutants. Vet Microbiol 1999;66(4):313–20.
[9] Compans RW, Mountcastle WE, Choppin PW. The sense of the helix of paramyxovirus nucleocapsids. J Mol Biol 1972;65(1):167–9.
[10] Heggeness MH, Scheid A, Choppin PW. The relationship of conformational changes in the Sendai virus nucleocapsid to proteolytic cleavage of the NP polypeptide. Virology 1981;114(2):555–62.
[11] Mountcastle WE, Compans RW, Lackland H, Choppin PW. Proteolytic cleavage of subunits of the nucleocapsid of the paramyxovirus simian virus 5. J Virol 1974;14(5):1253–61.
[12] Curran J, Homann H, Buchholz C, Rochat S, Neubert W, Kolakofsky D. The hypervariable C-terminal tail of the Sendai paramyxovirus nucleocapsid protein is required for template function but not for RNA encapsidation. J Virol 1993;67(7):4358–64.
[13] Nakamura J, Miyamoto T. Avianization of lapinized rinderpest virus. Am J Vet Res 1953;14(51):307–17.
[14] Morgan EM, Re GG, Kingsbury DW. Complete sequence of the Sendai virus NP gene from a cloned insert. Virology 1984;135(1):279–87.